Minimizing Structural Bias in Single-Molecule Super-Resolution Microscopy

Hesam Mazidi[1], Jin Lu[1], Arye Nehorai[1], and Matthew D. Lew[1,*]

[1]Department of Electrical and Systems Engineering, Washington University in St. Louis, MO 63130, USA
[*]Corresponding author: mdlew@wustl.edu

ABSTRACT

Single-molecule localization microscopy (SMLM) depends on sequential detection and localization of individual molecular blinking events. Due to the stochasticity of single-molecule blinking and the desire to improve SMLM's temporal resolution, algorithms capable of analyzing frames with a high density (HD) of active molecules, or molecules whose images overlap, are a prerequisite for accurate location measurements. Thus far, HD algorithms are evaluated using scalar metrics, such as root-mean-square error, that fail to quantify the *structure* of errors caused by the *structure* of the sample. Here, we show that the spatial distribution of localization errors within super-resolved images of biological structures are vectorial in nature, leading to systematic structural biases that severely degrade image resolution. We further demonstrate that the shape of the microscope's point-spread function (PSF) fundamentally affects the characteristics of imaging artifacts. We built a Robust Statistical Estimation algorithm (RoSE) to minimize these biases for arbitrary structures and PSFs. RoSE accomplishes this minimization by estimating the likelihood of blinking events to localize molecules more accurately and eliminate false localizations. Using RoSE, we measure the distance between crossing microtubules, quantify the morphology of and separation between vesicles, and obtain robust recovery using diverse 3D PSFs with unmatched accuracy compared to state-of-the-art algorithms.

Introduction

Since its invention, fluorescence imaging has been an indispensable tool for biological studies of cells, tissues, and organisms because of its ability to visualize specific molecules of interest against a dark background in a relatively noninvasive manner. Tagging a biological molecule with a small organic fluorophore or fluorescent protein enables a fluorescence microscope to produce pictures of structures and movies of interactions between molecules within living cells. The optical detection of individual fluorescent molecules in condensed matter[1] is the basis for an entire family of super-resolved fluorescence microscopy techniques[2–5]. These methods rely upon the blinking of fluorescent molecules in time to reduce the concentration of active emitters and resolve each molecule in a microscope image[6–8]. Repeated cycles of molecular blinking and measurement of molecular positions from their point spread functions (PSFs) by an image analysis algorithm result in reconstructed images of a biological structure with resolution beyond the Abbé diffraction limit ($\sim \lambda/2NA \approx 250$ nm for visible light, where NA is the numerical aperture of the fluorescence microscope). Here, we refer to these techniques collectively as single-molecule localization microscopy (SMLM).

Although the experimenter often chooses imaging conditions to minimize the probability of image overlap between two molecules, the stochasticity of molecular blinking often leads to some overlap in SMLM datasets, especially for complex biological structures with high fluorophore labeling density[9]. One may even purposefully increase the density of active fluorescent probes in any given camera acquisition, such that images of neighboring molecules frequently or regularly overlap, in order to improve the temporal resolution of SMLM. Consequently, fewer imaging frames are needed to reconstruct a target structure, thereby leading to decreased phototoxicity as well as a reduction in motion-blur artifacts[10,11].

From a statistical perspective, super-resolution imaging in the presence of significant image overlap poses two major problems: (i) identifying the underlying molecules, and (ii) estimating their positions and brightnesses. Strategies for resolving overlapping molecules are primarily based on two aspects of prior knowledge: molecules are sparsely distributed in space, and they repeatedly and independently blink over time[12]. The first strategy recasts the estimation of molecular positions as a sparse recovery optimization problem, where a sparsity prior regulates the solution[13,14]. The second approach exploits molecular emission characteristics (e.g., uncorrelated and repeated blinking events from various molecules) by applying higher-order statistics[15,16] or Bayesian analysis[17] on the images of blinking molecules.

Extracting quantities from SMLM images, such as distances between structures or the size and shape of nanodomains, require molecular estimates with high *precision*, i.e., having a minimal spread around the mean, as well as high *accuracy*, i.e., having a mean with minimal deviation from the true value[11,18]. In low-density (LD) SMLM, analyzing repeated and isolated

images of molecules guarantees statistically-unbiased estimates[19]. In particular, localization errors, i.e., the vectors obtained by taking the difference between true and estimated positions, are randomly distributed primarily due to Poisson shot noise. Consequently, the super-resolved images from a sufficiently large number of localizations are faithful representations of the ground truth, as long as systematic inaccuracies due to model PSF mismatch[11,20,21], aberration[22], and insufficient labeling[23] are properly removed. These statistical results, however, no longer apply when analyzing high-density (HD) images. For example, standard LD algorithms, although capable of resolving two closely-spaced molecules, underestimate their separation distance[24], suggesting that the localization errors are skewed toward neighboring molecules. This systematic bias gradually decreases as the separation distance becomes larger, achieving a minimum value beyond an algorithm-dependent distance[24]. In fact, the cumulative error between a super-resolution image reconstructed by a recovery algorithm and its ground truth scales exponentially with the degree of PSF overlap[25]; that is, the error increases as $c^{2\beta}$, where c is some constant and β, a regularity parameter, describes how many molecules actively emit light within a diffraction-limited region at any point in time.

Because the structure of interest dictates the regularity in the position of labeling molecules, these theoretical results imply that the extent and characteristics of reconstruction errors fundamentally depend on the said structure. Put differently, accuracy is no longer a scalar quantity but a *vectorial* one. We refer to systematic inaccuracies caused by the structure of the sample as *structural bias* (see Supplementary Information, section 1 for a precise definition). Metrics used to evaluate SMLM algorithms, such as root-mean-square error (RMSE), detection rate[26], and Pearson's correlation[16], collapse the reconstruction errors into a single number; moreover, visibility analysis only quantifies measurement precision, not accuracy[16]. These metrics, however, fail to fully characterize the vectorial nature of errors and ensuing biases. Errors caused by overlapping images become more severe in 3D SMLM, where 3D PSFs are larger than their 2D counterparts and are used to localize molecules over a larger domain[27]. More importantly, 3D super-resolution methods utilize diverse encoding mechanisms for depth, and a recovery algorithm that can be easily adapted to different PSFs is currently lacking.

Herein, we present a Robust Statistical Estimation algorithm, termed RoSE, for HD super-resolution imaging with arbitrary PSFs. In contrast to prior HD algorithms, RoSE jointly recovers molecular position and brightness through a novel optimization framework, allowing for estimating the likelihood that photons in the SMLM dataset arise from true molecular blinking events. The likelihoods are mapped into a tensor, termed GradMap, using vectors of estimated position gradients and molecular brightnesses. By leveraging (i) the spatial sparsity in molecular positions or equivalently in the GradMap to identify closely-spaced molecules; and (ii) the statistics of molecular blinking events to eliminate false localizations, RoSE achieves robust recovery against arbitrary image overlap due to sample structure and PSF.

We apply RoSE to recover realistic, bio-inspired structures in 2D (microtubules and densely-packed vesicles[23]) *in silico*. Our analysis reveals a sample-dependent bias for HD imaging and shows that RoSE reduces these structural biases compared to state-of-the-art algorithms. Notably, our analysis shows that scalar metrics such as RMSE and visibility are insufficient in quantifying the sample-dependent errors present in super-resolution images. Finally, we show how the structure of both the sample and the 3D PSF itself fundamentally affect the systematic inaccuracies in reconstructing dense arrangements of nuclear pore complexes *in silico* and demonstrate the robustness of RoSE in adapting to various 3D PSFs, namely the double-helix[28] and tetrapod[29,30] PSFs.

Results

Theory

A joint signal model

Localizing single molecules with overlapping images is in general a continuous recovery problem: molecular positions lie within a continuous range rather than a discrete set of points. If low-frequency Fourier samples of the signal are available, the total variation norm can be used to resolve two point sources with a certain separation by solving a convex program in the finite domain[31]. However, solving the continuous optimization problem for a general imaging model is not tractable. Beyond localization, estimating the brightness of fluorescence bursts plays a critical role for measuring molecular orientation[32].

To address these challenges, we propose a joint signal model in which we consider a single molecule as an isotropic point source and assume that within each frame, no two molecules emit within a certain neighborhood. (This model can be easily extended to include the emission anisotropy of dipole emitters by including molecular orientation[33].) Thus, each molecule within an image can be mapped to a unique nearest discrete grid point, each associated with a brightness and a set of position gradients (Fig. 1(a)). This signal model allows us to explicitly decouple the number of photons that a molecule emits from its continuous position, thus providing a robust estimator of these quantities with sub-pixel accuracy. In addition, these estimates can be exploited for temporal analysis, which is discarded by other signal models[13,14]. This signal model together with a first-order approximation result in a linear forward model with a convex set of constraints on molecular parameters, denoted by

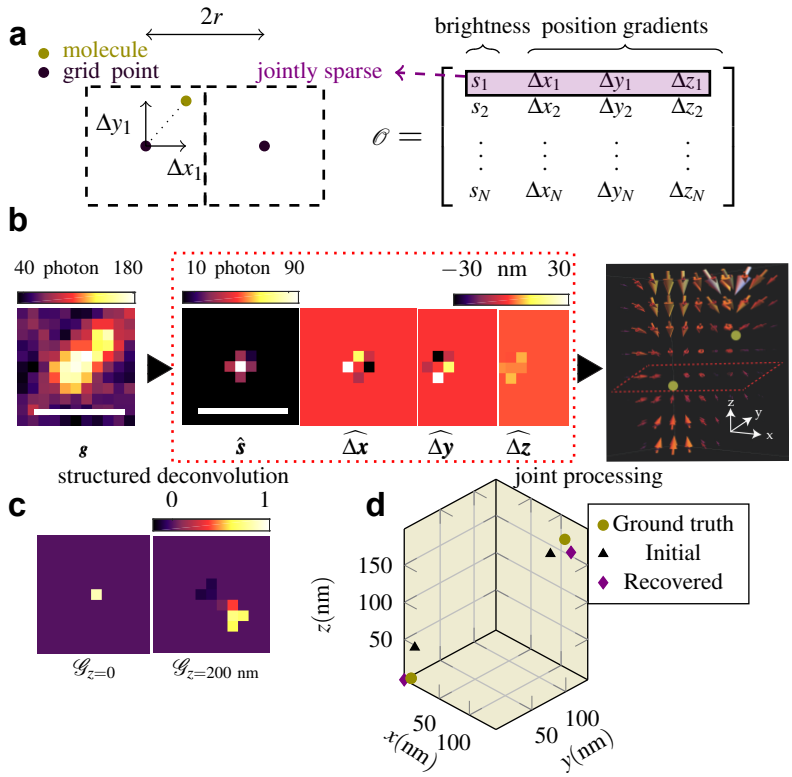

Figure 1. Joint recovery of molecular position and brightness by RoSE. (a) Left: Mapping of a continuous molecular position to a discrete grid in 2D ($r_x = r_y = r$). Right: Molecular parameters $\mathscr{O} = [\boldsymbol{s}, \boldsymbol{\Delta x}, \boldsymbol{\Delta y}, \boldsymbol{\Delta z}]$ in 3D. (b) Left: Simulated image of two overlapping molecules, located at $(0,0,0)$ and $(120,120,180)$ nm using the tetrapod PSF. Middle: Slices of recovered parameters $\hat{\mathscr{O}} = [\hat{\boldsymbol{s}}, \widehat{\boldsymbol{\Delta x}}, \widehat{\boldsymbol{\Delta y}}, \widehat{\boldsymbol{\Delta z}}]$ by (2) in the $z = 0$ plane. Right: Joint processing of brightness and position gradients of $\hat{\mathscr{O}}$ reveals two molecules unambiguously separated in 3D space (gold points). (c) Slices of estimated GradMap at $z = 0$ and $z = 200$ nm for the recovered signal in (b). (d) Initial position estimates (black triangles) obtained via the GradMap in (c), and the recovered molecular positions (purple diamonds) after applying adaptive constrained maximum likelihood. Ground-truth molecular positions are denoted by gold circles. Scale bars: 500 nm.

$\mathscr{O} \in \mathbb{R}^{N\times 4}$ (see Supplementary Information, section 2):

$$\begin{aligned} &\boldsymbol{g} = \boldsymbol{A\gamma}, \quad \boldsymbol{A} = [\boldsymbol{\Phi},\ \boldsymbol{G}_x \boldsymbol{G}_y, \boldsymbol{G}_z], \\ &\boldsymbol{\gamma} = [\boldsymbol{s}^T,\ \boldsymbol{s}^T \odot \boldsymbol{\Delta x}^T,\ \boldsymbol{s}^T \odot \boldsymbol{\Delta y}^T,\ \boldsymbol{s}^T \odot \boldsymbol{\Delta z}^T]^T = [\boldsymbol{s}^T, \boldsymbol{p}_x^T, \boldsymbol{p}_y^T, \boldsymbol{p}_z^T], \\ &\mathscr{C} = \{s_i \geq 0, -s_i r_j \leq p_{j,i} < s_i r_j, \quad i \in \{1,\ldots,N\},\ j \in \{x,y,z\}\}, \end{aligned} \tag{1}$$

where $\boldsymbol{g} \in \mathbb{R}^m$ represents the vectorized noiseless image relayed by the microscope; $\boldsymbol{\Phi} \in \mathbb{R}^{m\times N}$ denotes the PSF matrix sampled at the grid points; $\boldsymbol{G}_x \in \mathbb{R}^{m\times N}$, $\boldsymbol{G}_y \in \mathbb{R}^{m\times N}$, and $\boldsymbol{G}_z \in \mathbb{R}^{m\times N}$ represent corresponding gradient matrices along x, y, and z, respectively; N is the number of object grid points; and m is the number of image pixels. Further, $\boldsymbol{s} \in \mathbb{R}^N$ is the vectorized brightness and $\boldsymbol{\Delta x} \in \mathbb{R}^N$, $\boldsymbol{\Delta y} \in \mathbb{R}^N$, and $\boldsymbol{\Delta z} \in \mathbb{R}^N$ are the corresponding PSF gradient vectors ($\odot$ represents component-wise multiplication of two vectors) at each grid point. Additionally, $\mathscr{C}$ represents the convex set of constraints for a box centered at each grid point i with side lengths $2r_x$, $2r_y$, and $2r_z$ (Fig. 1(a)).

Identifying single molecules via structured deconvolution

We develop a structured deconvolution program to identify single molecules from their overlapping images. Our key insight is that the brightnesses $\boldsymbol{s}$ and position gradients $(\boldsymbol{G}_x, \boldsymbol{G}_y, \boldsymbol{G}_z)$ are jointly sparse. That is, if the brightness of a molecule associated with a grid point is zero (i.e., there is no molecule at that grid point), then the corresponding position gradients should be zero. (It is not strictly necessary for position gradients to be zero, however, these degenerate cases do not carry any physical information). The structured deconvolution is cast as an optimization problem:

$$\min_{\boldsymbol{\gamma}\in\mathscr{C}} \mathscr{L}(\boldsymbol{\gamma}, \boldsymbol{A}; \boldsymbol{g}, \boldsymbol{b}) + \lambda \|\boldsymbol{\gamma}\|_{1,2}, \tag{2}$$

where $\boldsymbol{b} \in \mathbb{R}^m$ is the vectorized background and λ is a sparsity penalty parameter. Further, $\mathscr{L}(\cdot)$ is the Poisson negative log likelihood and $\|\cdot\|_{1,2}$ denotes the mixed $\ell_{1,2}$ norm to enforce joint sparsity in $\boldsymbol{\gamma}$. The optimization problem given by (2) is a convex program (see Supplementary Information, section 3), and we develop a novel variant of the accelerated proximal gradient algorithm to efficiently solve it[34]. To calculate λ, we devised a computational tuning strategy (see Supplementary Information, section 3) that takes the PSF $\boldsymbol{\Phi}$ into account.

Fig. 1(b) illustrates a 3D example of two closely-spaced molecules with significantly-overlapping images. The recovered molecular parameters from (2) denoted by $\hat{\mathscr{O}} = [\hat{\boldsymbol{s}}, \widehat{\boldsymbol{\Delta x}}, \widehat{\boldsymbol{\Delta y}}, \widehat{\boldsymbol{\Delta z}}]$ cannot resolve the brightnesses and positions of the two molecules. However, examining the joint structure of $\hat{\mathscr{O}}$ reveals that the brightness-weighted position gradients converge to the 3D positions of each molecule (Fig. 1(b), right). To make this mapping precise, we define a tensor $\mathscr{G}$, called GradMap, in which each pixel takes on a value in $[-1, 1]$, termed the source coefficient, that signifies the local degree of convergence to that pixel (see Supplementary Information, section 3). In other words, the GradMap represents the likelihood that photons localized to particular positions in the map truly originate from the structure. Notably, GradMap leverages the convergent symmetry of the position gradients, thus sidestepping the need for PSF symmetry[16,35]. Consequently, the number of molecules and their initial parameters are estimated from the local maxima of GradMap (Fig. 1(c)).

Accurate and precise recovery via adaptive maximum likelihood

After identifying the correct number of molecules, we further minimize the errors due to sparsity constraint[14] as well as the sample's structure. Importantly, the magnitude of errors from conventional sparse deconvolution programs, which may be larger than a few grid points, depends on the underlying molecular positions[25]. For accurate and precise estimates, RoSE adaptively updates the grid point closest to the current estimate of the molecule's position (Fig. 1(d)) by maximizing adaptively a constrained maximum likelihood (see Supplementary Information, section 3). This strategy enhances the accuracy of both molecular position and brightness estimates and attains the limits of precision indicated by Cramér-Rao bound (CRB) (Fig. S2-S6).

Exploiting temporal blinking statistics via GradMap

Since molecular blinking events occur stochastically, misidentified localizations resulting from overlapping images exhibit significantly less autocorrelation over time compared to molecules that are accurately identified. Thus, the autocorrelated GradMap represents the confidence that molecules represent the true structure and not a false localization (see Supplementary Information, section 3). Noting that GradMap localizes these blinking events with sub-pixel accuracy, we apply a threshold on the pixel-wise temporal autocorrelation of GradMap to eliminate false localizations. We refer to this scheme as RoSE-C.

Beyond Scalar Metrics

Traditional performance metrics for evaluating HD recovery algorithms, such as recall rate (i.e., the number of molecules that are recovered correctly with a certain distance criteria) and the RMSE between correctly recovered molecules and their matched ground truths[26], disregard the role of underlying structure; the magnitude and direction of errors vary across the super-resolved image. Moreover, the visibility of the structure (i.e., the ratio between peak brightness of a pair of structures to the brightness of the dimmest position between them) cannot quantify imaging accuracy[16]. In the following sections, we examine and characterize the structural biases of various recovery algorithms by simulating realistic, HD SMLM image stacks of several bio-inspired structures.

Accurate frame-by-frame analysis: imaging crossing microtubules using RoSE

To quantitatively characterize the effects of sample structure and blinking density on the size and structure of localization errors, we construct and examine two crossing microtubules (MTs) *in silico*. MTs are tubular intracellular assemblies of the protein tubulin that form a dynamic, three-dimensional network[36]. MTs act as "robotic arms" and are responsible for key functions such as cell division, shaping the cell membrane, and intracellular transport[36].

The MTs are simulated as cylinders aligned perpendicular to the optical axis with radii of 12.5 nm and are displaced symmetrically about the focal plane with an axial separation of 25 nm. We consider a uniform labeling density of 0.04 molecules/nm^2 on the surface of the cylinders. A continuous temporal emission model (see Supplementary Information, section 4) accounts for stochastic nature of molecular emission. The labeling density together with the temporal emission characteristics, e.g., on rate and mean switching time, impose a mean blinking density, which represents the average number of active molecules per the area occupied by the sample. For each molecule, we generated photon counts per burst according to a Poisson distribution whose mean is proportional to a chosen emission brightness. We model photon emission without photobleaching in order to directly test algorithmic performance and avoid image artifacts from insufficient sampling of the biological structure[23]. Additionally, the number of frames is selected such that each molecule blinks on average once, which ensures an asymptotic statistical performance analysis.

To measure the mean separation between MTs, we consider a sliding rectangular area containing both MTs with a constant 58.5-nm height (Fig. 2(a) orange box). The rectangle is sufficiently large such that labeling noise is insignificant but small

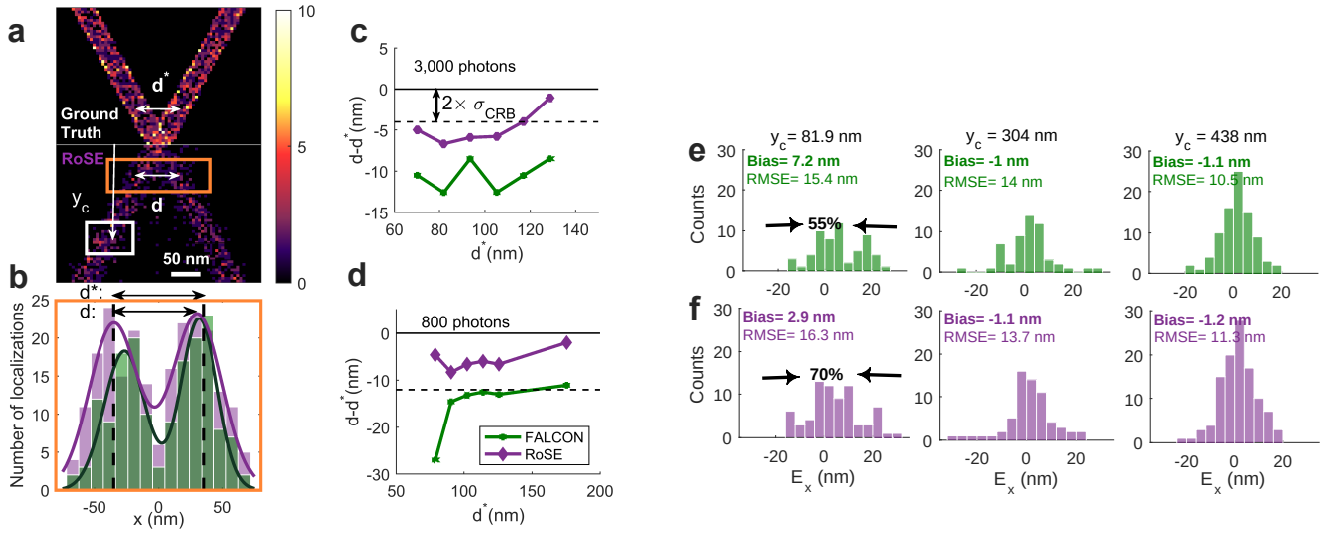

Figure 2. Structural bias of two crossing microtubules recovered by RoSE (purple) and FALCON (green). (a) 2D histogram of (top) the simulated ground-truth structure and (bottom) recovered structural obtained by RoSE for a blinking density of 1.3×10^{-5} molecules/nm^2 (color bar: number of localizations per 5×5 nm^2). (b) Projection of the localizations within the orange box in (a) and the corresponding double Gaussian fits. The arrows labeled by d^* and d denote the distance between the centers of the two microtubules, and the distance between the peaks of the fitted double Gaussian, respectively. (c,d) Mean distance between centers of the microtubules along the length of the structure for a blinking density of 1.3×10^{-5} molecules/nm^2 and mean emission intensities of (c) 3000 photons and (d) 800 photons. (e,f) Localization errors along the +x direction (E_x) for molecules within the white box in (a) at various distances from the center crossing y_c: (left) 81.9 nm , (middle) 304 nm, (right) 438 nm. The noted bias values represent the difference between the true center of the MT and the mean of matched localizations; the arrows indicate a $[10, -10]$ nm interval centered at the true position of the MT.

enough to resolve algorithm performance as a function of true separation d^*. The localizations within the rectangular area are then projected onto the x-axis transverse to the MTs, collapsing the localization data into histograms.

We tested RoSE and FALCON[14], of which the latter has a high accuracy score (low RMSE) and a competitive Jaccard index[26], on image data generated at various blinking densities, namely 4.9×10^{-6}, 1.3×10^{-5}, and 1.9×10^{-5} molecules/nm^2, representing low, high, and ultra-high densities, respectively (Fig. S7). At high blinking density, the measured mean separation distance exhibits a negative bias for both algorithms, meaning errors are structured toward the center of the MTs (Fig. 2(b)). Compared to FALCON, RoSE reduces the bias in measuring d^* across the entire length of the structure, and the measured errors drop to being CRB-limited more quickly for RoSE than FALCON for both low (800 photons) and high (3000 photons) molecular brightnesses (Fig. 2(c),(d)). In particular, for true mean separations from 70.2 nm to 128.7 nm (Fig. 2(c)), RoSE incurs an average bias of -4.7 nm compared to -10.5 nm for FALCON. This difference in average bias becomes more pronounced for dimmer molecules (Fig. 2(d)), where RoSE exhibits a small bias of -5.7 nm, which is well within the FWHM of the theoretical limit of precision ($\approx 2.3 \times \sigma_{\mathrm{CRB}} = 13.8$ nm). In contrast, FALCON incurs an average bias of -15.2 nm. For large d^*, the error distance is non-zero due to non-uniform sampling and stochastic localization precision.

Examining the left-most MT at various distances y_c from the crossing point reveals the vectorial nature of these errors (Fig. 2(e,f)). We calculated the localization error E_x along the x dimension by matching correctly-identified localizations to the ground-truth dataset[26] (see Supplementary Information, section 5). Interestingly when $y_c = 81.9$ nm, the errors are skewed toward +x direction (Fig. 2(e)), in accord with the systematic underestimates of MT separation (Fig. 2(c,d)). As y_c increases, the distribution of the error converges to a Gaussian distribution centered at zero whose width is determined by the CRB, as expected. This analysis reveals an important consequence of misidentifying the number of molecules present in a given image. In a region where local blinking density is high, FALCON underestimates the number of molecules near the center of the MT crossing (Fig. S7(d)). To compensate for this error, FALCON mislocalizes the molecules it does identify, with errors as large as 68 nm oriented towards the center crossing. In contrast, RoSE is able to localize a molecule at the crossing center and exhibits smaller localization errors overall.

RMSE analysis cannot reveal such a structural bias, i.e., the systematic deviation of localized molecules away from the true center of the MT. Surprisingly, the RMSE for FALCON is slightly smaller than RoSE for $y_c = 81.9$ nm (Fig. 2(e,f) left); however, the percentage of localized molecules for RoSE that are within $[-10, 10]$ nm is 70% compared to 55% for FALCON;

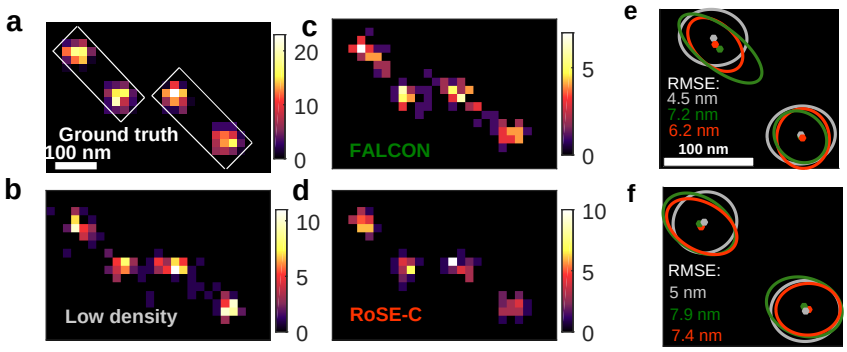

Figure 3. Structural bias in the sizes and shapes of vesicles recovered by RoSE-C and FALCON. (a) Simulated ground-truth structure of 4 circular vesicles each with radius of 30 nm, uniformly labeled with a labeling density of 0.035 molecules/nm^2. The mean emission intensity and mean uniform background were set to 800 photons and 40 photons per pixel, respectively. (b) Structure recovered from low-density frames using ThunderSTORM. (c) Structure recovered by FALCON. (d) Structure recovered by RoSE-C. Color bars: number of localizations per 19.5×19.5 nm^2. (e,f) Estimated clusters, their confidence ellipses, and the RMSE of all localizations corresponding to the (e) left and (f) right boxes in (a) for low-density imaging (grey), FALCON (green), and RoSE-C (orange), respectively.

this increased localization accuracy results in more accurate measurements of the MT separation distance (Fig. 2(b)). Indeed, the Jaccard index calculated over the entire structure for RoSE (54%) is higher than FALCON (49%). These results suggest that decomposing the reconstruction errors into scalar detection and localization error metrics cannot quantify the variation in magnitudes as well as vectorial nature of these significant biases. Therefore, a structure-based analysis of errors beyond scalar metrics is critical for quantitative evaluation and insight into the performance of recovery algorithms.

Additionally, RoSE maintains its robust performance and consistently outperforms FALCON at both low and higher blinking densities. Even at low blinking density, RoSE resolves the walls of MTs with much better visibility than FALCON (57% larger), especially close to the crossing point (Fig. S7).

Leveraging blinking statistics across frames: accurate imaging of vesicles via RoSE-C

SMLM techniques have revealed the morphology of protein clusters within bacteria[37] and during the assembly of HIV viruses[38]. In particular, clustering algorithms have been utilized to infer clusters and their spatial distributions from SMLM datasets[18]. The accuracy of such analyses, however, critically relies upon the accuracy of positions output from the SMLM algorithm.

We examine the structural errors in characterizing clusters from simulated SMLM data of a dense arrangement of fluorescently-labeled vesicles. These four vesicles are modeled as circles with a 30 nm radius, each uniformly labeled with 100 molecules. These molecules blink within a total of 80 frames (a mean blinking density of 4.7×10^{-5} molecules/nm^2), resulting in highly-overlapped images and a short acquisition time. To separate Poisson shot noise and sampling artifacts, we compared reconstructions from this HD dataset to equivalent LD imaging (i.e., one burst per frame with the same brightness as in HD data) in which no image overlaps. ThunderSTORM was chosen to provide a super-resolved structure from LD frames[39].

We tested the performance of RoSE-C in eliminating false localizations that mostly occur between vesicles due to significant image overlap. Remarkably, RoSE-C perfectly restores the discrete structure of packed vesicles for various signal-to-background levels as well as blinking densities (Fig. S8). Computing the confidence level of obtaining true localizations, quantified by the auto-correlated GradMap, critically enables RoSE-C to filter out false localizations otherwise recovered by RoSE.

ThunderSTORM, FALCON, and RoSE-C are all able to resolve 4 clusters (Fig. 3(a-d)). The sizes and shapes of these vesicles were analyzed using a density-based clustering algorithm, which takes into account vesicle size and localization precision and is robust against false localizations[40] (see Supplementary Information, section 5). The two left-most clusters for ThunderSTORM (Fig. 3(b,e)) exhibit a small average ellipticity of 1.2, defined by the ratio of the major axis and the minor axis, and similarly the two right-most clusters (Fig. 3(b,f)) have an average ellipticity of 1.12. These small ellipticity values could be caused by Poisson shot noise and finite-sampling artifacts. Interestingly, the clusters for both RoSE-C and FALCON (Fig. 3(c-f)) are skewed toward neighboring vesicles, and exhibit larger ellipticity values. The two left-most clusters recovered by RoSE-C (Fig. 3(d,e)) exhibit an average ellipticity of 1.38 ($\{\text{major}, \text{minor}\}$ axes lengths of $\{36, 22\}$ and $\{33, 29\}$ nm), while for FALCON (Fig. 3(c,e)), the average ellipticity is 1.84 (axes lengths of $\{55, 22\}$ and $\{31, 26\}$ nm). For the two right-most clusters, RoSE-C (Fig. 3(d,f)) has a slightly smaller average ellipticity of 1.42 (axes lengths of $\{44, 27\}$ and $\{37, 30\}$ nm) compared to FALCON's (Fig. 3(c,f)) 1.44 (axes lengths of $\{46, 30\}$ and $\{45, 33\}$ nm). Overall RoSE-C minimizes the average ellipticity bias by 24%. This analysis reveals vectorial inaccuracies (i.e., structured ellipticity) present in the super-resolved

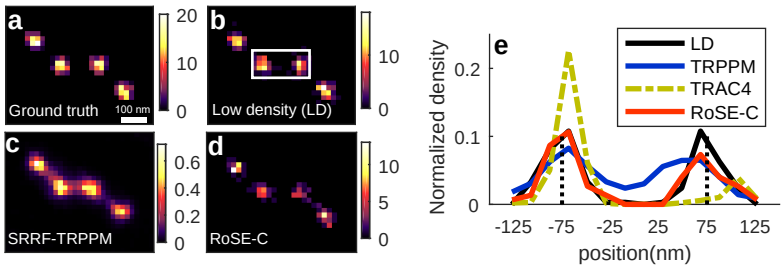

Figure 4. Bias in measuring vesicle separation and labeling density. (a) Simulated ground-truth structure of four uniformly-labeled vesicles. The mean emission intensity and mean uniform background were set to 3000 photons and 40 photons per pixel, respectively. (b) Structure recovered from low-density (LD) frames using ThunderSTORM. (c) Density map recovered by SRRF-TRPPM. (d) Structure recovered by RoSE-C. Color bars: (a,b,d) number of localizations per 19.5×19.5 nm^2, (c) normalized labeling density. (e) 1D profile of the two middle vesicles (box in (b)) projected onto the x axis for LD, SRRF (TRPPM and TRAC4), and RoSE-C. Dotted lines denote the true centers of the two vesicles.

images that cannot be fully quantified by scalar RMSE values.

Recently, a class of algorithms termed super-resolution radial fluctuations (SRRF)[16] was introduced based on super-resolution optical fluctuation imaging (SOFI)[15]. SRRF relies on radial symmetry (spatial information) to reduce the apparent FWHM of the Gaussian PSF. Moreover, by applying higher-order statistics to images of blinking molecules over time, SRRF resolves molecules at smaller separations with better visibility.

We next quantify the separation and relative density of recovered vesicles (i.e., the number of blinking events or brightness of each vesicle) from simulated SMLM datasets. A low-density (LD) dataset containing 4 vesicles uniformly-labeled with blinking molecules (Fig. 4(a)) was analyzed by ThunderSTORM (Fig. 4(b)), while RoSE-C (Fig. 4(c)) and SRRF (Fig. 4(d)) analyzed a HD dataset with the same total number of blinking events. To measure the separation between two vesicles, the localizations within the region of interest (see box in Fig. 4(b)) were projected onto the x axis and normalized relative to the total number of localizations.

The projected profiles of the two vesicles (Fig. 4(e)) remarkably show the robustness of RoSE-C in accurately resolving the distance between vesicles (-5 nm bias or -3%) and their relative densities with a normalized visibility of 1 compared to LD imaging (separation bias $= 0.5$ nm (0.3%) and normalized visibility = 1). SRRF-TRPPM, which applies pixel-wise autocorrelation on radiality maps, has a poor visibility of 0.64. Importantly, it exhibits a bias of -20 nm (-13%) in measuring the separation distance. SRRF-TRAC4, which applies a fourth-order autocumulant, increases the normalized visibility to 1. However, it incurs a bias of $+40$ nm (27%) in measuring the separation between vesicles and exhibits a significant bias in estimated labeling density. Interestingly, the arrangement of vesicles affects the accuracy of each SRRF algorithm differently due to non-zero cross-correlation terms in the cumulant analysis[16] (Fig. S9). This analysis reveals that the apparent visibility between structures, which is unity for SRRF-TRAC2, TRAC3, and TRAC4, ignores the structural biases present in both estimated position and labeling density.

Because the accuracy of cumulant analysis and pixel-wise-correlation improves with an increasing number of uncorrelated frames[41], we have performed simulations to separate the structural errors from those that are due to an insufficient number of blinking events. Surprisingly, even when each activated molecule blinks, on average, 4.8 times over 480 frames, the central vesicles appear to shift $+20$ nm toward the right-most vesicle for SRRF-TRAC4 (Fig. S10). This shift is minimal for both LD imaging (-8 nm) and RoSE-C (-9 nm). Additionally, SRRF-TRAC4 overestimates the average labeling density of the two left-most vesicles by 20%, while it underestimates the labeling density of the right-most ones by 18% (Fig. S11). These observations show that localization errors and biases in measuring labeling density affect one another.

Robust 3D recovery using diverse PSFs

PSF engineering has become a popular strategy for 3D super-resolution imaging. A variety of PSFs, including the astigmatic PSF[42], the double-helix PSF (DH-PSF)[28], and the tetrapod PSF[29,30] can be implemented with fixed phase masks or programmable hardware. These PSFs have tunable axial ranges (spanning $2-20$ μm[27]) and exhibit diverse and complex features over their measurement domains. Importantly, they occupy more space on the camera compared to the standard PSF. Therefore, addressing the problem of image overlap for an arbitrary 3D PSF becomes critical.

We test the robustness of RoSE-C in recovering dense arrangements of nuclear pore complexes (NPCs) in 3D using the DH and tetrapod PSFs. An NPC is a ring-like protein complex composed of eight subunits with an approximate diameter of 90-120 nm, well below the diffraction limit[43]. The complex and dense 3D arrangements of NPCs necessitate the use of 3D super-resolution techniques for measuring their diameters and resolving their subunits[44]. We simulated each NPC

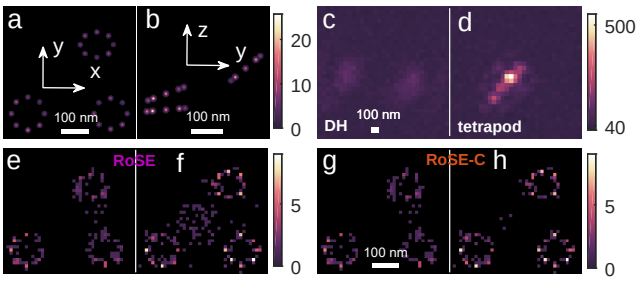

Figure 5. 3D recovery of densely-packed NPCs using the double-helix and tetrapod PSFs. (a) xy and (b) yz views of the simulated ground-truth arrangement of 3 NPCs centered at $(0,0,0),(300,0,50)$, and $(200,200,130)$ nm, each consisting of 8 labeling sites equidistantly distributed on a circle with diameter of 120 nm. The brightest pixel corresponds to the peak of a Gaussian distribution (standard deviation = 3.5 nm) multiplied by the number of blinking events. (c,d) Representative images of overlapping molecules corresponding to the (c) DH and (d) tetrapod PSFs. (e,f) xy projections of the NPCs recovered by RoSE using the (e) DH and (f) tetrapod PSFs. (g,h) xy projections of the NPCs recovered by RoSE-C using the (g) DH and (h) tetrapod PSFs. Color bars: (a,b) number of blinking events/nm^2; (c,d) number of photons per 58.5×58.5 nm^2; and (e-h) number of localizations per 12×12 nm^2.

using 8 subunits equidistantly distributed on a circle with a diameter of 120 nm. The NPCs are placed in 3D with centers at $(0,0,0),(300,0,50)$, and $(200,200,130)$ nm with various orientations (Fig. 5(a,b)). Each subunit is labeled with a single fluorophore that blinks stochastically with a mean brightness of 3100 photons per blinking event. On average, one molecule per NPC emits during any specific frame, causing a high probability of PSF overlap on the camera (Fig. 5(c,d)).

In the projected 2D images of the NPCs recovered by RoSE, the NPC subunits are more blurry when using the DH-PSF (Fig. 5(e)) compared to the tetrapod (Fig. 5(f)). This difference is consistent with the superior precision of the tetrapod PSF[29], which allows for counting subunits using the clustering algorithm with 25% better accuracy (see Fig. S12 for the performance of the DH and tetrapod PSFs in resolving two closely-spaced molecules). Intriguingly, however, the super-resolved structure by RoSE using the tetrapod PSF exhibits a set of mislocalizations at higher axial coordinates resembling an NPC (Fig. 5(f)). In contrast, there are fewer mislocalizations in the reconstruction using the DH-PSF, and interestingly, they do not resemble an NPC (Fig. 5(e)).

RoSE-C remarkably minimizes the structured mislocalizations when using the tetrapod PSF (Fig. 5(h)). This improved accuracy is enabled by GradMap, in which pixels that correspond to false localizations exhibit smaller autocorrelation over time than those that correspond to true localizations (Fig. S13). For the DH-PSF, the mislocalizations between the two right-most NPCs cannot be eliminated with RoSE-C. One possible reason is that the pixel size of the GradMap (58.5 nm) is larger than the half of the separation between the two right-most NPCs along the y dimension (120 nm). Thus, in this particular simulation, GradMap has insufficient spatial sampling to resolve false localizations from true ones using temporal autocorrelation.

To gather insight into the structured mislocalizations in the recovered NPCs using the tetrapod PSF, we consider overlapping images of molecules located within a small volume $[-60,\ 290] \times [14,\ 219] \times [70,\ 470]$ nm^3. The image (Fig. S14) generated by a set of molecules with various brightnesses and positions can be closely approximated by another set of molecules of distinct brightnesses and positions. This example illustrates a high degree of linear dependency[45] of tetrapod PSF sampled within a relatively small region; that is, multiple arrangements of molecules can generate very similar images on the camera.

This degeneracy fundamentally limits the performance of any sparse recovery algorithm[45]: it is easier to recover the true signal if there is a small degree of linear dependence between the columns of the PSF matrix A. If there is a large degree of linear dependence, then accurate recovery is not guaranteed. However, these theoretical results do not reveal the role of the structure itself influencing the bias. We examined a different arrangement with NPCs located at $(0,0,0),(300,0,50)$, and $(200,200,-130)$ nm using the tetrapod PSF. Surprisingly, the number of mislocalizations in the super-resolved structure by RoSE is significantly reduced (Fig. S13). This reduction likely results from the distinct depth encoding of negative z values compared to positive ones for the tetrapod PSF. Thus, the tetrapod can resolve NPCs accurately when they are alternate sides of the focal plane rather than all above the focal plane.

Discussion

The *vectorial* nature of localization errors in SMLM is often ignored. Our simulations show that when recovering bio-inspired structures under HD imaging conditions, reconstruction errors exhibit magnitudes and directions that depend on the structure of the sample and cannot be revealed by conventional error metrics. Furthermore, in 3D SMLM, the inaccuracies are affected both

by the *structure* of the sample and the *structure* of the PSF. In particular, PSF degeneracy causes structured mislocalizations that may pose difficulty for downstream quantitative analysis[18].

Current methods for minimizing nanoscale inaccuracies, including classifying localizations based on spot size, brightness[24], and similarity-based techniques[46], lack robustness against sample structure and become unreliable for 3D imaging. The structure of the sample and heterogeneity in emission intensity affect the characteristics of overlapped PSFs, thus making it difficult to robustly identify false localizations on the basis of an image's features without prior knowledge of the structure. A simple classifier that rejects localizations whose corresponding images overlap may unnecessarily reduce the number of useful localizations in the resulting SMLM dataset[24]. For instance, localization errors due to overlapping PSFs in the regions far from the center of the crossing MTs are mostly along the length of MTs (Fig. 2). Therefore, these biased localizations still reveal information about the MT's structure and can be utilized for reconstruction. Further, point-wise precision for individual localizations, which is used for filtering localizations with large uncertainty, becomes inaccurate in the case of overlapping PSFs due to biased brightness estimates (Fig. S4). Taken together, these observations necessitate estimation of a fundamentally different quantity for individual localizations.

RoSE addresses these challenges by directly estimating the likelihood of fluorescence emission for individual blinking events, which enables molecules with overlapping images to be localized in the continuous domain and increases localization and photon-counting accuracy. Further by assuming that the sample structure is stationary over the imaging interval, RoSE-C simply autocorrelates these likelihoods to obtain point-wise confidence levels without knowing the sample structure *a priori*. The confidence level of a localization signifies its uncertainty in representing the ground truth, which is exploited to eliminate false localizations at higher blinking densities (Fig. S8). More importantly, the estimated confidence levels do not rely on point-wise precision, brightness, or how molecules' images overlap and can be applied to any arbitrary PSF. Access to such a confidence metric is a key to automating challenging quantitative analyses in SMLM, such as elucidating protein organization in 3D.

We emphasize that although RoSE-C eliminates localizations with small confidence levels, which may degrade the overall apparent labeling density, these localizations would otherwise lead to structural biases if they are not eliminated. This degradation in HD SMLM is fundamentally different from low-density SMLM for which even localizations with large uncertainty provide unbiased information regarding the underlying structure. Besides thresholding, the confidence levels can systematically be used as additional input to increase the accuracy of various quantitative analyses such as Bayesian clustering[47]. Nonetheless, RoSE-C exhibits robustness in measuring the apparent labeling density w.r.t. the number of blinking events per molecule, whereas image-based HD algorithms utilizing higher-order statistics incur significant errors (Fig. S11). Finally, we note that, at ultra-high molecular blinking densities, the pixel-wise autocorrelation produces confidence levels for false localizations that rise above our chosen threshold (Fig. S8). A more effective approach in this situation may be to exploit the spatial correlation in the GradMap stack. Investigating an optimal strategy for leveraging correlations between multiple blinking events remains the subject of future studies.

References

1. Moerner, W. E. & Kador, L. Optical detection and spectroscopy of single molecules in a solid. *Phys. Rev. Lett.* **62**, 2535–2538 (1989). DOI 10.1103/PhysRevLett.62.2535.
2. Betzig, E. *et al.* Imaging intracellular fluorescent proteins at nanometer resolution. *Science.* **313**, 1642–1645 (2006). DOI 10.1126/science.1127344.
3. Hess, S. T., Girirajan, T. P. & Mason, M. D. Ultra-High Resolution Imaging by Fluorescence Photoactivation Localization Microscopy. *Biophys. J.* **91**, 4258–4272 (2006). DOI 10.1529/biophysj.106.091116.
4. Rust, M. J., Bates, M. & Zhuang, X. Sub-diffraction-limit imaging by stochastic optical reconstruction microscopy (STORM). *Nat. Methods* **3**, 793–796 (2006). DOI 10.1038/nmeth929.
5. Sharonov, A. & Hochstrasser, R. M. Wide-field subdiffraction imaging by accumulated binding of diffusing probes. *Proc. Natl. Acad. Sci. USA* **103**, 18911–18916 (2006). DOI 10.1073/pnas.0609643104.
6. Betzig, E. Single Molecules, Cells, and Super-Resolution Optics (Nobel Lecture). *Angewandte Chemie Int. Ed.* **54**, 8034–8053 (2015). DOI 10.1002/anie.201501003.
7. Hell, S. W. Nanoscopy with Focused Light (Nobel Lecture). *Angewandte Chemie Int. Ed.* **54**, 8054–8066 (2015). DOI 10.1002/anie.201504181.
8. Moerner, W. E. Single-Molecule Spectroscopy, Imaging, and Photocontrol: Foundations for Super-Resolution Microscopy (Nobel Lecture). *Angewandte Chemie Int. Ed.* **54**, 8067–8093 (2015). DOI 10.1002/anie.201501949.
9. Burgert, A., Letschert, S., Doose, S. & Sauer, M. Artifacts in single-molecule localization microscopy. *Histochem. cell biology* **144**, 123–131 (2015).

10. Wäldchen, S., Lehmann, J., Klein, T., van de Linde, S. & Sauer, M. Light-induced cell damage in live-cell super-resolution microscopy. *Sci. Reports* **5**, 15348 (2015). DOI 10.1038/srep15348.

11. Deschout, H. *et al.* Precisely and accurately localizing single emitters in fluorescence microscopy. *Nat. Methods* **11**, 253–266 (2014).

12. Annibale, P., Vanni, S., Scarselli, M., Rothlisberger, U. & Radenovic, A. Quantitative Photo Activated Localization Microscopy: Unraveling the effects of photoblinking. *PLoS ONE* **6**, e22678 (2011). DOI 10.1371/journal.pone.0022678.

13. Zhu, L., Zhang, W., Elnatan, D. & Huang, B. Faster STORM using compressed sensing. *Nat. Methods* **9**, 721–723 (2012).

14. Min, J. *et al.* FALCON: fast and unbiased reconstruction of high-density super-resolution microscopy data. *Sci. Reports* **4**, 4577 (2015). DOI 10.1038/srep04577.

15. Dertinger, T., Colyer, R., Iyer, G., Weiss, S. & Enderlein, J. Fast, background-free, 3D super-resolution optical fluctuation imaging (SOFI). *Proc. Natl. Acad. Sci. USA* **106**, 22287–22292 (2009).

16. Gustafsson, N. *et al.* Fast live-cell conventional fluorophore nanoscopy with ImageJ through super-resolution radial fluctuations. *Nat. Commun.* **7**, 12471 (2016). DOI 10.1038/ncomms12471.

17. Cox, S. *et al.* Bayesian localization microscopy reveals nanoscale podosome dynamics. *Nat. Methods* **9**, 195–200 (2012). DOI 10.1038/nmeth.1812.

18. Nicovich, P. R., Owen, D. M. & Gaus, K. Turning single-molecule localization microscopy into a quantitative bioanalytical tool. *Nat. Protoc.* **12**, 453–461 (2017). DOI 10.1038/nprot.2016.166.

19. Ober, R. J., Ram, S. & Ward, E. S. Localization Accuracy in Single-Molecule Microscopy. *Biophys. J.* **86**, 1185–1200 (2004). DOI 10.1016/S0006-3495(04)74193-4.

20. Abraham, A. V., Ram, S., Chao, J., Ward, E. S. & Ober, R. J. Quantitative study of single molecule location estimation techniques. *Opt. express* **17**, 23352–73 (2009). DOI 10.1364/OE.17.023352.

21. Stallinga, S. & Rieger, B. Accuracy of the Gaussian Point Spread Function model in 2D localization microscopy. *Opt. Express* **18**, 24461 (2010). DOI 10.1364/OE.18.024461.

22. Von Diezmann, A., Lee, M. Y., Lew, M. D. & Moerner, W. E. Correcting field-dependent aberrations with nanoscale accuracy in three-dimensional single-molecule localization microscopy. *Optica.* **2**, 985–993 (2015).

23. Venkataramani, V., Herrmannsdörfer, F., Heilemann, M. & Kuner, T. SuReSim: simulating localization microscopy experiments from ground truth models. *Nat. Methods* **13**, 319–321 (2016).

24. Fox-Roberts, P. *et al.* Local dimensionality determines imaging speed in localization microscopy. *Nat. Commun.* **8**, 13558 (2017). DOI 10.1038/ncomms13558.

25. Morgenshtern, V. I. & Candes, E. J. Super-resolution of positive sources: The discrete setup. *SIAM J. on Imaging Sci.* **9**, 412–444 (2016).

26. Sage, D. *et al.* Quantitative evaluation of software packages for single-molecule localization microscopy. *Nat. Methods* **12**, 1–12 (2015). DOI 10.1038/nmeth.3442.

27. Von Diezmann, A., Shechtman, Y. & Moerner, W. E. Three-Dimensional Localization of Single Molecules for Super-Resolution Imaging and Single-Particle Tracking. *Chem. Rev.* **117**, 7244–7275 (2017). DOI 10.1021/acs.chemrev.6b00629.

28. Pavani, S. R. P. *et al.* Three-dimensional, single-molecule fluorescence imaging beyond the diffraction limit by using a double-helix point spread function. *Proc. Natl. Acad. Sci. USA* **106**, 2995–2999 (2009).

29. Shechtman, Y., Sahl, S. J., Backer, A. S. & Moerner, W. E. Optimal point spread function design for 3d imaging. *Phys. Rev. Lett.* **113**, 133902 (2014).

30. Shechtman, Y., Weiss, L. E., Backer, A. S., Sahl, S. J. & Moerner, W. E. Precise three-dimensional scan-free multiple-particle tracking over large axial ranges with tetrapod point spread functions. *Nano Lett.* **15**, 4194–4199 (2015).

31. Candès, E. J. & Fernandez-Granda, C. Towards a mathematical theory of super-resolution. *Commun. on Pure Appl. Math.* **67**, 906–956 (2014).

32. Backlund, M. P. *et al.* Simultaneous, accurate measurement of the 3d position and orientation of single molecules. *Proc. Natl. Acad. Sci. USA* **109**, 19087–19092 (2012).

33. Backer, A. S. & Moerner, W. E. Extending Single-Molecule Microscopy Using Optical Fourier Processing. *J. Phys. Chem. B* **118**, 8313–8329 (2014). URL http://pubs.acs.org/doi/10.1021/jp501778z. DOI 10.1021/jp501778z.

34. Beck, A. & Teboulle, M. A fast iterative shrinkage-thresholding algorithm for linear inverse problems. *SIAM J. on Imaging Sci.* **2**, 183–202 (2009).

35. Parthasarathy, R. Rapid, accurate particle tracking by calculation of radial symmetry centers. *Nat. Methods* **9**, 724–726 (2012).

36. Hess, H. & Ross, J. L. Non-equilibrium assembly of microtubules: from molecules to autonomous chemical robots. *Chem. Soc. Rev.* **46**, 5570–5587 (2017). DOI 10.1039/C7CS00030H.

37. Lee, S. F., Thompson, M. A., Schwartz, M. A., Shapiro, L. & Moerner, W. E. Super-resolution imaging of the nucleoid-associated protein HU in Caulobacter crescentus. *Biophys. J.* **100**, L31–L33 (2011).

38. Gunzenhäuser, J., Olivier, N., Pengo, T. & Manley, S. Quantitative super-resolution imaging reveals protein stoichiometry and nanoscale morphology of assembling HIV-gag virions. *Nano Lett.* **12**, 4705–4710 (2012). DOI 10.1021/nl3021076.

39. Ovesný, M., Křížek, P., Borkovec, J., Švindrych, Z. & Hagen, G. M. ThunderSTORM: A comprehensive ImageJ plug-in for PALM and STORM data analysis and super-resolution imaging. *Bioinformatics.* **30**, 2389–2390 (2014). DOI 10.1093/bioinformatics/btu202.

40. Ehmann, N. *et al.* Quantitative super-resolution imaging of Bruchpilot distinguishes active zone states. *Nat. Commun.* **5**, 4650 (2014). DOI 10.1038/ncomms5650.

41. Wang, X., Chen, D., Yu, B. & Niu, H. Statistical precision in super-resolution optical fluctuation imaging. *Appl. Opt.* **55**, 7911–7916 (2016).

42. Huang, B., Wang, W., Bates, M. & Zhuang, X. Three-dimensional super-resolution imaging by stochastic optical reconstruction microscopy. *Science.* **319**, 810–813 (2008).

43. Szymborska, A. *et al.* Nuclear Pore Scaffold Structure Analyzed by Super-Resolution Microscopy and Particle Averaging. *Science.* **341**, 655–658 (2013). DOI 10.1126/science.1240672.

44. Huang, F. *et al.* Ultra-high resolution 3D imaging of whole cells. *Cell* **166**, 1028–1040 (2016).

45. Bruckstein, A. M., Donoho, D. L. & Elad, M. From sparse solutions of systems of equations to sparse modeling of signals and images. *SIAM review* **51**, 34–81 (2009).

46. Culley, S. *et al.* Quantitative mapping and minimization of super-resolution optical imaging artifacts. *Nat. methods* (2018). DOI 10.1038/nmeth.4605.

47. Rubin-Delanchy, P. *et al.* Bayesian cluster identification in single-molecule localization microscopy data. *Nat. Methods* **12**, 1072–1076 (2015). DOI 10.1038/nmeth.3612.

Data Availability

Ground-truth molecule brightnesses and positions, simulated noisy images, and brightness and localization data output by RoSE and RoSE-C are available at: https://osf.io/vbptf/?view_only=5947ca1b9e8948bca2c70e536314d43d

Acknowledgements

We thank Yoav Shechtman for providing the tetrapod PSF and Tianben Ding, Oumeng Zhang, and Zhenqi Lu for their feedback on the manuscript. Research reported in this publication was supported by the National Science Foundation under grant number ECCS-1653777 and by the National Institute of General Medical Sciences of the National Institutes of Health under grant number R35GM124858 to M.D.L.

Author contributions statement

H.M., A.N., and M.D.L. conceived the research; H.M. designed and wrote RoSE algorithm; H.M. designed and conducted the *in slilico* studies with input from J.L. and M.D.L.; A.N. and M.D.L. supervised the research; All authors co-wrote and reviewed the manuscript.

Additional information

Competing financial interests: The authors declare that they have no competing interests.